Published in final edited form as:
Int j numer method biomed eng. 2013 November ; 29(11): 1267–1284. doi:10.1002/cnm.2575.

Modeling the dispersion in electromechanically coupled myocardium

Thomas S. E. Eriksson[1,2], **Anton J. Prassl**[2], **Gernot Plank**[2], and **Gerhard A. Holzapfel**[1,3,*,†]

[1]Institute of Biomechanics, Center of Biomedical Engineering, Graz University of Technology, 8010 Graz, Austria

[2]Department of Biophysics, Medical University of Graz, 8010 Graz, Austria

[3]Department of Solid Mechanics, School of Engineering Sciences, Royal Institute of Technology (KTH), Teknikringen 8d, 100 44 Stockholm, Sweden

SUMMARY

We present an approach to model the dispersion of fiber and sheet orientations in the myocardium. By utilizing structure parameters, an existing orthotropic and invariant-based constitutive model developed to describe the passive behavior of the myocardium is augmented. Two dispersion parameters are fitted to experimentally observed angular dispersion data of the myocardial tissue. Computations are performed on a unit myocardium tissue cube and on a slice of the left ventricle indicating that the dispersion parameter has an effect on the myocardial deformation and stress development. The use of fiber dispersions relating to a pathological myocardium had a rather big effect. The final example represents an ellipsoidal model of the left ventricle indicating the influence of fiber and sheet dispersions upon contraction over a cardiac cycle. Although only a minor shift in the pressure–volume (PV) loops between the cases with no dispersions and with fiber and sheet dispersions for a healthy myocardium was observed, a remarkably different behavior is obtained with a fiber dispersion relating to a diseased myocardium. In future simulations, this dispersion model for myocardial tissue may advantageously be used together with models of, for example, growth and remodeling of various cardiac diseases.

Keywords

computational biomechanics; dispersion; myocardium; electromechanical coupling

1. INTRODUCTION

The left ventricle (LV) is the main pumping chamber of the heart supplying blood through the circulatory system to the entire body. The LV builds up the necessary pressure by active contraction where the electrical activation of the heart triggers a cascade of events leading to a shortening of the cardiac myocytes. Myocytes are arranged in a highly organized fashion, following a right-handed helical pathway from the endocardium toward the mid-wall and a left-handed helical pathway from the mid-wall toward the epicardium [1-3]. This prevailing myocyte orientation is usually referred to as ‘fiber orientation’. In addition, fiber bundles are arranged into laminar sheets of four to six cell layers, where the prevailing sheet orientation

*Correspondence to: Gerhard A. Holzapfel, Graz University of Technology, Institute of Biomechanics, Center of Biomedical Engineering, Kronesgasse 5-I, 8010 Graz, Austria.
†holzapfel@tugraz.at

Europe PMC Funders Author Manuscripts

also varies in the transmural and apico-basal directions [3-6]. At any point in the LV, the structural arrangement of myocytes is reflected by three orthogonal directions along which both electrical and mechanical material parameters are different, thus requiring to model the electrical and mechanical responses of the myocardium as an *orthotropic* material. These preferred directions are along the fibers, transverse to the fibers but within a laminar sheet and perpendicular to the sheets; these directions are thus called the fiber, sheet, and sheet-normal directions, respectively.

In a healthy heart, the fiber alignment follows very closely this helical structure with only small angular dispersion (AD) in the range of ~ 12–15°, whereas in a diseased heart such as hypertrophic cardiomyopathy (HCM) or myocardial infarction, AD may locally increase by ~ 65% (at foci points within the septal wall) [7-9] or ~ 50% (at the site of infarction) [10-12]. Furthermore, the dispersion of the fibers has been shown to have a circular distribution, they are not located in plane [13]. Less is known about the structural arrangement of laminae. Because of the importance of sheet orientation in myocardial wall thickening, it has been speculated that the dispersion of sheet orientations may play a significant physiological role [14]. There are a few studies available discussing the quite large dispersion of the sheet structure, even in healthy hearts [15-17]. Although to our knowledge there are no experimental reports available that quantify sheet dispersion in the diseased myocardium, it is likely the case that dispersion is also elevated when compared with healthy conditions. To the authors' knowledge, there are no recently published biomechanical cardiac models available that consider dispersion, the latest are [2, 9]; none of them include sheet dispersion. Hence, the present study focuses on the development of an approach to model fiber and sheet dispersions using an invariant-based framework. A previously published orthotropic and invariant-based model, which characterizes the nonlinear passive behavior of myocardium [18], is here augmented with structure parameters allowing the quantification of the degree of dispersion based on measured fiber and sheet angle data. The structure parameters are based on a distribution function developed for the collagen structure of arteries [19], and is here used for the fiber and sheet dispersions.

Cardiac simulations have electrical and mechanical components rendering the modeling to a multi-physics problem. Electromechanical models need high spatiotemporal resolution, making the entire problem computationally expensive; advanced numerics and highly optimized parallel implementations are needed to keep simulations tractable. Therefore, a natural choice is the use of overlapping grids of different resolution because the constraints differ significantly between the imposed physics of the electrical and mechanical problems. The electrical transients are fast, acting on time scales in the microsecond range, which translates into steep depolarization wavefronts of small spatial extent in the sub-millimeter range, thus requiring the use of fine spatial resolutions << 250 μm to compute solutions with reasonable accuracy. On the other hand, mechanical processes tend to occur at larger space and slower time scales, and, thus, coarser spatial discretizations can be used. The electromechanical coupling of the spatiotemporal patterns of the electrical activity and the active stress transients in the myocytes are either modeled as active stresses or strains [20] acting along the fiber's orientation in an Eulerian description [21]. The resulting mechanical deformations in our model is largely determined by the passive hyperelastic properties of the tissue and the generated active stresses both incorporating the dispersed structure of the tissue.

Our simulation indicates that the dispersion has a relevant influence on the mechanical response of the myocardium both during passive deformation and active contraction, by reducing the stress response and changing the deformation pattern. When including the dispersion parameter in a ventricular simulation incorporating electrical activation, the

pressure–volume (PV) loop is considerably altered. Because the degree of dispersion is significantly elevated under various cardiac pathologies there is a need to consider dispersion when modeling myocardial tissue in diseased states.

2. MODELING FRAMEWORK

2.1. Kinematics

The structure of the myocardium may be described by three orthogonal direction vectors $\mathbf{f}_0$, $\mathbf{s}_0$, and $\mathbf{n}_0$ corresponding to the mean fiber, sheet, and sheet-normal directions, respectively, in the Lagrangian description (Figure 1). In a continuum setting, this fiber and sheet direction vectors are considered as averaged quantities over several fibers and sheets.

The isochoric Eulerian counterpart of these direction vectors are given by the relations $\bar{\mathbf{f}} = \mathbf{J}^{-1/3}\mathbf{F}\mathbf{f}_0$, $\bar{\mathbf{s}} = \mathbf{J}^{-1/3}\mathbf{F}\mathbf{s}_0$ and $\bar{\mathbf{n}} = \mathbf{J}^{-1/3}\mathbf{F}\mathbf{n}_0$, where $\mathbf{F}$ is the deformation gradient, and $J = \det\mathbf{F} > 0$ is the volume ratio. The displacement field $\mathbf{u}$ between the two points $\mathbf{X}$ and $\mathbf{x}$ at time t is given by $\mathbf{u} = \mathbf{x} - \mathbf{X}(\mathbf{x}, t)$. The circular dispersion of the fiber and sheet direction vectors around their mean orientations may be modeled using the structure tensors

$$\mathbf{H}_\mathrm{f} = \kappa_\mathrm{f}\mathbf{I} + (1 - 3\kappa_\mathrm{f})\,\mathbf{f}_0 \otimes \mathbf{f}_0, \quad \mathbf{H}_\mathrm{s} = \kappa_\mathrm{s}\mathbf{I} + (1 - 3\kappa_\mathrm{s})\,\mathbf{s}_0 \otimes \mathbf{s}_0, \quad (1)$$

$$\bar{\mathbf{h}}_\mathrm{f} = \kappa_\mathrm{f}\,\bar{\mathbf{b}} + (1 - 3\kappa_\mathrm{f})\,\bar{\mathbf{f}} \otimes \bar{\mathbf{f}}, \quad \bar{\mathbf{h}}_\mathrm{s} = \kappa_\mathrm{s}\,\bar{\mathbf{b}} + (1 - 3\kappa_\mathrm{s})\,\bar{\mathbf{s}} \otimes \bar{\mathbf{s}}, \quad (2)$$

as similarly described in [19], where $\mathbf{H}_i$ are Lagrangian structure tensors and $\bar{\mathbf{h}}_i = J^{-2/3}\mathbf{F}\mathbf{H}_i\mathbf{F}^\mathrm{T}$ are isochoric Eulerian structure tensors, where $i \in \{\mathrm{f}, \mathrm{s}\}$ correlates to the fiber and sheet directions. The second-order identity tensor is denoted by $\mathbf{I}$ while the modified isochoric left Cauchy Green tensor is denoted by $\bar{\mathbf{b}} = \mathbf{J}^{-2/3}\mathbf{F}\mathbf{F}^\mathrm{T}$.

The formulation of the dispersion parameters κ_i is described in detail in [19]. Briefly, the range of valid values for κ_i are $\in [0, 1/3]$, where $\kappa_i = 0$ means perfect alignment and $\kappa_i = 1/3$ means isotropy. A formulation of κ_i may be derived through the probability density function (PDF) $\rho_i(\Theta)$, using the relation

$$\kappa_i = \frac{1}{4}\int_0^\pi \rho_i(\Theta)\sin^3\Theta \mathrm{d}\Theta \quad (3)$$

where, Θ is the distribution angle centered around, $\Theta = 0$. We assume that the fiber and sheet dispersions follow a transversely isotropic and standard π-periodic von Mises distribution, which is modified in order to satisfy the normalization condition [19,22]. The PDF is, thus, given by

$$\rho(\Theta) = 4\sqrt{\frac{b_\rho}{2\pi}}\frac{\exp\{b_\rho[\cos(2\Theta)+1]\}}{\mathrm{erfi}\left(\sqrt{2b_\rho}\right)} \quad (4)$$

where b_ρ is a concentration parameter and $\mathrm{erfi}(x) = -i\,\mathrm{erf}(x)$ denotes an imaginary error function. The function $\rho(\Theta)$ is the standard π-periodic von Mises PDF, normalized by

$$\frac{1}{4\pi}\int_\omega \rho(\Theta)\,\mathrm{d}\omega = 1 \quad (5)$$

where ω is the unit sphere.

The values for κ_i may thus be fitted to the histograms of the dispersion of fiber and sheet angles for the myocardial tissue. To fit the PDF (4) to histogram data (fiber angles), the fiber angle Θ is shifted to $\bar{\Theta}$ to center around, $\Theta = 0°$ (the bar on the Θ variable denotes the shifted value), and the maximum likelihood method in MATLAB, that is, *mle()*, is used together with a custom function describing Equation (4). The parameter b_ρ is thus retrieved with a 95% confidence interval, and by using (3), the parameters κ_i are obtained. The one-to-one relation between the concentration parameter b_ρ and the dispersion parameter κ_i is discussed in detail in [19,22], where it is shown that $\kappa \to 1/3$ as $b_\rho \to 0$ and $\kappa \to 0$ as $b_\rho \to \infty$.

The fit of the PDF to the fiber dispersion is shown in Figure 2 for both a healthy myocardial tissue (see Figure 2(a)), and a diseased tissue (see Figure 2(b)), where the dispersion data were adapted from [7]. The fit of the PDF to the sheet dispersion is only shown for a healthy sub-epicardium (see Figure 2(c)), where the dispersion data were adapted from [16]. To the authors' knowledge, the structure of sheet orientations in a diseased myocardium has never been investigated. The fitting produced the dispersion parameters $\kappa_f = 0.00765$ and $\kappa_s = 0.0249$ for the healthy myocardial tissue and $\kappa_f = 0.0886$ for the diseased tissue; compare with Figure 2.

In the proposed framework, the dispersion parameters for the fiber and sheet directions are uncoupled, and we assume that the mean orientation of these directions are kept orthogonal. Furthermore, the dispersion of the sheet-normal direction is not considered; it is excluded to match the strain-energy function developed in [18], as shown in Section 2.2.

2.2. Constitutive relations

The anisotropy, generated by the preferred directions of the material (Figure 1), can be modeled by using the isochoric invariants $\bar{I}_{4\mathrm{f}} = \mathbf{f}_0 \cdot \bar{\mathbf{C}}\mathbf{f}_0$, $\bar{I}_{4\mathrm{s}} = \mathbf{s}_0 \cdot \bar{\mathbf{C}}\mathbf{s}_0$ and $\bar{I}_{4\mathrm{n}} = \mathbf{n}_0 \cdot \bar{\mathbf{C}}\mathbf{n}_0$, where $\bar{\mathbf{C}} = J^{-2/3}\mathbf{C}$ is the modified right Cauchy–Green tensor, and $\mathbf{C} = \mathbf{F}^{\mathrm{T}}\mathbf{F}$ denotes the right Cauchy–Green tensor [23].

By using the first invariant of $\bar{\mathbf{C}}$, namely, $\bar{I}_1 = \bar{\mathbf{C}}:\mathbf{I}$, we may define the two modified invariants $\bar{I}^*_{4\mathrm{f}}$ and $\bar{I}^*_{4\mathrm{s}}$ as a linear combination of $\bar{I}_1$, $\bar{I}_{4\mathrm{f}}$ and $\bar{I}_{4\mathrm{s}}$. Thus,

$$\bar{I}^*_{4i} = \kappa_i \bar{I}_1 + (1 - 3\kappa_i)\,\bar{I}_{4i}, \quad i \in \{\mathrm{f}, \mathrm{s}\} \tag{6}$$

similar to [19, 22, 24]. To characterize the orthotropic behavior of the myocardium, we modify the strain-energy function suggested by Holzapfel & Ogden [18] by writing

$$\Psi = U(J) + \bar{\Psi}_{\mathrm{p}}\left(\bar{I}_1, \bar{I}^*_{4\mathrm{f}}, \bar{I}^*_{4\mathrm{s}}, \bar{I}_{8\mathrm{fs}}\right) \tag{7}$$

where $\bar{I}_{8\mathrm{fs}} = \mathbf{f}_0 \cdot \bar{\mathbf{C}}\mathbf{s}_0$ is the modified invariant which couples $\mathbf{f}_0$ with $\mathbf{s}_0$, U is a volumetric function, and $\bar{\Psi}_{\mathrm{p}}$ is an isochoric strain-energy function describing the passive behavior of the myocardium. For the volumetric function, we use

$$U(J) = \frac{\mu_{\mathrm{K}}}{2}(\ln J)^2 \tag{8}$$

where μ_{K} serves as a user-specified penalty parameter. In an analogous manner to [18], the isochoric strain-energy function for the passive myocardium tissue is given by

$$\overline{\Psi}_{\mathrm{p}}=\frac{a}{2b}\left\{\exp\left[b\left(\bar{I}_1-3\right)\right]-1\right\}+\sum_{i=\mathrm{f,s}}\frac{a_i}{2b_i}\left\{\exp\left[b_i\left(\bar{I}^{*}_{4i}-1\right)^2\right]-1\right\}+\frac{a_{\mathrm{fs}}}{2b_{\mathrm{fs}}}\left[\exp\left(b_{\mathrm{fs}}\bar{I}^{2}_{8\mathrm{fs}}\right)-1\right] \quad (9)$$

Note that in the limiting case, where $\kappa_i = 0$, the original model, as described in [18], is retrieved.

The material parameters needed in (8) and (9) are μ_{K}, a, b, $a_{(\mathrm{f,\,s,\,fs})}$ and $b_{(\mathrm{f,\,s,\,fs})}$ and the two dispersion parameters κ_{f} and κ_{s}. The passive Cauchy stress tensor is given by $\sigma_{\mathrm{p}} = 2J^{-1}\mathbf{F}(\partial\Psi/\partial\mathbf{C})\mathbf{F}^{\mathrm{T}}$, and by using the notation

$$\overline{\psi}_j=\frac{\partial\overline{\Psi}_{\mathrm{p}}}{\partial\bar{I}_j},\quad j=1,8\mathrm{fs},\qquad \overline{\psi}^{*}_{4i}=\frac{\partial\overline{\Psi}_{\mathrm{p}}}{\partial\bar{I}^{*}_{4i}},\quad i=\mathrm{f,s} \quad (10)$$

this results into

$$\sigma_{\mathrm{p}}=p_{\mathrm{h}}\mathbf{I}+2J^{-1}\left[\overline{\psi}_1\mathrm{dev}\,\bar{\mathbf{b}}+\sum_{i=\mathrm{f,s}}\overline{\psi}^{*}_{4i}\,\mathrm{dev}\bar{\mathbf{h}}_i+\frac{1}{2}\overline{\psi}_{8\mathrm{fs}}\,\mathrm{dev}\left(\bar{\mathbf{f}}\otimes\bar{\mathbf{s}}+\bar{\mathbf{s}}\otimes\bar{\mathbf{f}}\right)\right] \quad (11)$$

where $p_{\mathrm{h}} = \mathrm{d}U(J)/\mathrm{d}J$ is used, and $\mathrm{dev}(\bullet) = (\bullet) - (1/3)[(\bullet) : \mathbf{I}]\mathbf{I}$ denotes the deviatoric operator in Eulerian [23].

The evolution of an active second Piola–Kirchhoff stress term S_{a}, which originates from [25], is given by

$$\frac{\partial S_{\mathrm{a}}}{\partial t}=\epsilon\left(V_{\mathrm{m}}\right)\left(k_{S_{\mathrm{a}}}\Delta V_{\mathrm{m}}-S_{\mathrm{a}}\right) \quad (12)$$

where $\epsilon(V_{\mathrm{m}})$ is a delay function controlling the rate of activation and relaxation of S_{a}. The parameter $k_{S_{\mathrm{a}}}$ regulates the amplitude of S_{a}, $\Delta V_m = V_{\mathrm{m}} - V_{\mathrm{r}}$ is the difference in the transmembrane potential, where V_{m} is the current action potential, and V_{r} is the myocyte resting potential. A smooth delay function $\epsilon = \epsilon(V_{\mathrm{m}})$, as proposed in [26], is used, which is given by

$$\epsilon\left(V_{\mathrm{m}}\right)=\epsilon_0+\left(\epsilon_\infty-\epsilon_0\right)\exp\left\{-\exp\left[-\zeta_{\mathrm{r}}\left(V_{\mathrm{m}}-V_{\mathrm{s}}\right)\right]\right\} \quad (13)$$

where ϵ_0 and ϵ_∞ are the limiting values of the delay function when the action potential V_{m} is larger or lower than a given phase shift V_{s}. Further, the transition rate of the delay function is controlled by the parameter ϵ_{r}. However, in contradiction to what is written in [26], the relation between the limiting values must follow $\epsilon_0 > \epsilon_\infty$ in order to achieve the delay of peak active stress with respect to the upstroke of the action potential. An active second Piola–Kirchhoff stress tensor $\mathbf{S}_{\mathrm{a}}$ is retrieved by introducing a dispersed structure tensor $\widehat{\mathbf{H}}_{\mathrm{a}}$ a according to

$$\mathbf{S}_{\mathrm{a}}=S_{\mathrm{a}}\widehat{\mathbf{H}}_{\mathrm{a}} \quad (14)$$

where

$$\widehat{\mathbf{H}}_{\mathrm{a}}=\frac{\kappa_{\mathrm{f}}}{1-2\kappa_{\mathrm{f}}}\mathbf{C}^{-1}+\frac{1-3\kappa_{\mathrm{f}}}{1-2\kappa_{\mathrm{f}}}I^{-1}_{4\mathrm{f}}\,\mathbf{f}_0\otimes\mathbf{f}_0 \quad (15)$$

Europe PMC Funders Author Manuscripts

with $I_{4\mathrm{f}} = J^{2/3}\bar{I}_{4\mathrm{f}}$. The active Cauchy stress tensor σ_a a is now retrieved by the push-forward operation according to $\sigma_\mathrm{a} = J^{-1}\mathbf{F}\mathbf{S}_\mathrm{a}\mathbf{F}^\mathrm{T}$, which yields

$$\sigma_\mathrm{a} = J^{-1} S_\mathrm{a} \widehat{\mathbf{h}}_\mathrm{a} \quad (16)$$

where

$$\widehat{\mathbf{h}}_\mathrm{a} = \frac{\kappa_\mathrm{f}}{1-2\kappa_\mathrm{f}}\mathbf{I} + \frac{1-3\kappa_\mathrm{f}}{1-2\kappa_\mathrm{f}}\,\widehat{\mathbf{f}} \otimes \widehat{\mathbf{f}} \quad (17)$$

where $\widehat{\mathbf{f}} = \mathbf{f}/|\mathbf{f}|$ is the normalized fiber direction vector. The structure tensor (15) is formulated so that (17) may be seen as a normalization of $(2)_1$ where the length change of the mean fiber orientation does not affect the magnitude of the applied stress so that the condition $\widehat{\mathbf{f}} \cdot \widehat{\mathbf{h}}_\mathrm{a}\widehat{\mathbf{f}} = \mathbf{1}$ holds, which together ensures that (16) is a true Cauchy stress tensor. The Cauchy stress tensor $\boldsymbol{\sigma}$ is now simply given by the additive decomposition

$$\sigma = \sigma_\mathrm{p} + \sigma_\mathrm{a} \quad (18)$$

The elasticity tensors needed for implementing the passive stress $\boldsymbol{\sigma}_\mathrm{p}$ in the finite element (FE) analysis program [27] have previously been shown in [19], and for the active stress σ_a, the elasticity tensor in the Lagrangian and the Eulerian descriptions is shown in the Appendix.

2.3. Modeling electromechanically coupled myocardial tissue

The computation of electrical activation and repolarization and their coupling to passive tissue mechanics is here briefly described. The spread of electrical activation and repolarization is described by a reaction–diffusion equation referred to as the mono-domain equation, given by

$$\beta C_\mathrm{m}\frac{\partial V_\mathrm{m}}{\partial t} + \beta I_\mathrm{ion}\left(V_\mathrm{m}, \eta\right) = \nabla \cdot \left(\mathbf{g}_\mathrm{m}\nabla V_\mathrm{m}\right) + I_\mathrm{tr} \quad (19)$$

where β is the membrane surface to volume ratio, C_m is the membrane capacitance, V_m is the transmembrane potential, I_ion is the density of the total ionic current which is a function of V_m and a set of state variables η, I_tr is the transmembrane stimulus current, and $\mathbf{g}_\mathrm{m}$ is the mono-domain conductivity tensor with the eigenaxes $\zeta = f$ along the fibers, $\zeta = s$ perpendicular to the fibers, but within a laminar sheet, and $\zeta = n$ is perpendicular to the sheets. No dispersion parameters are here included in the formulation of the electrical activation. The eigenvalues of $\mathbf{g}_\mathrm{m}$ are chosen as the harmonic mean of the intracellular and interstitial conductivities, which renders the mono-domain equation axially equivalent to the more general bi-domain equation [28,29].

We employ the FEM for the spatial discretization of the mono-domain equation (19). A ventricular geometry is modeled using two overlapping FE meshes, a fully structured coarser hexahedral mesh for solving the mechanics and a fully unstructured hybrid mesh with an average resolution of ~200 μm, using an image-based mesh generation technique [30], as implemented in the commercial mesh generator Tarantula (CAE Software Solution, Eggenberg, Austria) for solving electrics. Fiber and sheet orientations are interpolated onto the barycenters of the FEs in both meshes. Both grids were partitioned for parallel execution using parMETIS [31]. By treating the diffusion terms implicitly and the reaction terms explicitly, the temporal discretization of the mono-domain equation relies on an implicit–explicit scheme, using the time step of 20 s. Blocked Jacobi pre-conditioner with an iterative

Europe PMC Funders Author Manuscripts

conjugate gradient solver is used to solve the linear system in parallel, using an Incomplete LU (ILU(0)) factorization as a sub-block pre-conditioner [32].

The electrical and mechanical models are weakly coupled, that is, the solution of the electrical quantities (19) is calculated on a static mesh first, using the Cardiac Arrhythmia Research Package [33], which is built on top of the message passing interface-based library PETSc [32]. Numerical aspects of this approach have been described in detail elsewhere [34]. Relevant parameters, that is, V_m, required for computing the active stress transients are transferred to the integration points of the mechanical mesh and fed into a separate subsequent simulation of deformation and stress analysis using an FE analysis program [27].

In this study, however, the electrical quantities are either calculated according to (19), as is the case in the model of an LV, Section 3.5, or the transmembrane potential V_m is prescribed directly as an input to the mechanical deformation analysis.

3. REPRESENTATIVE NUMERICAL EXAMPLES

To illustrate the effect of the myocardial model considering dispersion, five representative numerical examples are carried out. In order to elucidate how the dispersion parameters κ_f and κ_s influence the myocardium model behavior, they are appropriately modified; for example, isotropic fiber distribution was considered while keeping a small dispersion in the sheet orientation and vice versa. Such relations between fiber and sheet dispersion are non-physiological but are used to provide more insight into the proposed model.

The five examples are as follows: (i) in Section 3.1, a unit cube of myocardial tissue is electrically activated to generate active tension. The influence of the dispersion on the mechanical deformation (stretch) is studied by varying the dispersion parameters κ_f and κ_s; (ii) a second example, see Section 3.2, aims to predict the influence of the dispersion on simple shear; (iii) an FE model of a cube of myocardial tissue is used in Section 3.3 to investigate the relative influence of electrically generated active stress in the presence of dispersion of the fiber orientation; (iv) in Section 3.4, a passive inflation experiment on a ventricular section is performed to study the transmural change in stress as a function of the altered dispersion parameters related to the fiber and sheet directions; and (v) an electromechanically coupled LV model is used in Section 3.5 to study the influence of fiber and sheet dispersions upon contraction on PV loops over a cardiac cycle where dispersion parameters are chosen to account for both healthy and pathological conditions.

The related numerical results were obtained by using mixed $Q1/P0$ displacement/pressure FEs.

3.1. Electrically activated cube with dispersion

A unit myocardium tissue cube with mean material directions is considered. By introducing a global coordinate system (X_1, X_2, X_3), the material directions are according to $[\mathbf{f}_0] = [1, 0, 0]^T$, $[\mathbf{s}_0] = [0, 1, 0]^T$, and $[\mathbf{n}_0] = [0, 0, 1]^T$. The cube is fixed against rigid body movement but can otherwise freely deform. The reference configuration of the cube is shown by the dashed lines in Figure 3(a). The cube is activated by increasing the transmembrane potential V_m generating a contraction in the fiber direction. The corresponding deformation gradient is given by $\mathbf{F} = \mathrm{diag}(\lambda_f, \lambda_s, \lambda_n)$, where λ_f, λ_s and λ_n are the stretches in the fiber, sheet, and sheet-normal directions, respectively. Because the activation in the fiber direction leads to a contraction of the fiber, the stretches follow the relations $\lambda_f < 1$, $\lambda_s > 1$, and $\lambda_n > 1$. A deformed configuration (at $V_m = 50$ mV, with $\kappa_f = \kappa_s = 0$) is shown by the solid lines in Figure 3(a). The components of the Cauchy stress tensor $\sigma = \sigma_p + \sigma_a$ can now be calculated from (11) and (16) by using $J = 1$. Thus,

$$\sigma_{11} = p_{\mathrm{h}} + 2\left[\overline{\psi}_1 + \overline{\psi}^*_{4\mathrm{f}}\left(1 - 2\kappa_{\mathrm{f}}\right) + \overline{\psi}^*_{4\mathrm{s}}\kappa_{\mathrm{s}}\right]\lambda_{\mathrm{f}}^2 + S_{\mathrm{a}} \quad (20)$$

$$\sigma_{22} = p_{\mathrm{h}} + 2\left[\overline{\psi}_1 + \overline{\psi}^*_{4\mathrm{f}}\kappa_{\mathrm{f}} + \overline{\psi}^*_{4\mathrm{s}}\left(1 - 2\kappa_{\mathrm{s}}\right)\right]\lambda_{\mathrm{s}}^2 + S_{\mathrm{a}}\frac{\kappa_{\mathrm{f}}}{1 - 2\kappa_{\mathrm{f}}} \quad (21)$$

$$\sigma_{33} = p_{\mathrm{h}} + 2\left(\overline{\psi}_1 + \overline{\psi}^*_{4\mathrm{f}}\kappa_{\mathrm{f}} + \overline{\psi}^*_{4\mathrm{s}}\kappa_{\mathrm{s}}\right)\lambda_{\mathrm{n}}^2 + S_{\mathrm{a}}\frac{\kappa_{\mathrm{f}}}{1 - 2\kappa_{\mathrm{f}}} \quad (22)$$

$$\sigma_{12} = \sigma_{13} = \sigma_{23} = 0 \quad (23)$$

Because the cube can freely deform, the stress components σ_{11}, σ_{22}, and σ_{33} are zero, and p_{h} may be determined by, for example, $\sigma_{33} = 0$. The unknowns are the stretches λ_{f}, λ_{s}, and λ_{n}. By the use of the incompressibility condition $\lambda_{\mathrm{f}}\lambda_{\mathrm{s}}\lambda_{\mathrm{n}} = 1$, the nonlinear system (20)–(22) can be solved with respect to λ_{f}, λ_{s} and λ_{n} by using the function *fsolve()* in MATLAB. The given values are the dispersion parameters κ_{f} and κ_{s} and the active stress S_{a} which is computed from the given transmembrane potential V_{m}.

With the material parameters from Table I and a linear increase in the transmembrane potential from $V_{\mathrm{m}} = V_{\mathrm{r}}$ to $V_{\mathrm{m}} = +50$ mV, the resulting stretches can be plotted as a function of the transmembrane potential V_{m}, see Figure 3(b,c) for different sets of the dispersion parameters κ_{f} and κ_{s}. The fiber, sheet, and sheet-normal responses are shown by solid, dashed, and dotted curves, respectively (the stretches in Figure 3 are abbreviated by λ). In addition, a comparison is shown with FE results obtained for the same model setup where $\kappa_{\mathrm{f}} = 1/6$ in Figure 3(b) and $\kappa_{\mathrm{s}} = 1/6$ in Figure 3(c) (the FE results are shown as circles). For the limiting case $\kappa_{\mathrm{f}} = 1/3$, the active stress acts in all direction, and due to the incompressibility, the cube cannot deform, resulting in a straight line at $\lambda = 1$ for all directions, as shown by the dash-dotted line in Figure 3(b). For the limiting case $\kappa_{\mathrm{s}} = 1/3$ (the sheet direction is isotropic), the stretch responses in the sheet and sheet-normal directions are shown by the dash-dotted curves in Figure 3(c). Note that the sheet and sheet-normal responses are indistinguishable. For $\kappa_{\mathrm{s}} = 1/3$, the material model can be viewed as transversely isotropic.

3.2. Influence of dispersion on simple shear

Consider the same unit myocardium tissue cube with the same material directions as formulated in the previous example but subjected to a simple shear deformation in the 21-plane caused by the deformation gradient $\mathbf{F} = \mathbf{I} + \gamma \mathbf{f}_0 \otimes \mathbf{s}_0$ (see Figure 4(a)). Thereby, γ denotes the amount of shear. In addition, let us consider a plane stress state throughout the myocardium tissue in the sense that the face of the cube normal to the direction $\mathbf{n}_0$ is free of surface traction ($\sigma_{13} = \sigma_{23} = \sigma_{33} = 0$). For that particular setup, the nonzero Cauchy stress components can be derived from (11) and (16). After some lengthy but straightforward computation, we obtain

$$\sigma_{11} = 2\left\{\overline{\psi}_1\gamma^2 + \overline{\psi}^*_{4\mathrm{f}}\left[1 + \left(\gamma^2 - 3\right)\kappa_{\mathrm{f}}\right] + \overline{\psi}^*_{4\mathrm{s}}\left(1 - 2\kappa_{\mathrm{s}}\right)\gamma^2 + \overline{\psi}_{8\mathrm{fs}}\gamma\right\} + S_{\mathrm{a}}\frac{1 - 3\kappa_{\mathrm{f}}}{1 - 2\kappa_{\mathrm{f}}} \quad (24)$$

$$\sigma_{22} = 2\overline{\psi}^*_{4\mathrm{s}}\left(1 - 3\kappa_{\mathrm{s}}\right) \quad (25)$$

Europe PMC Funders Author Manuscripts

$$\sigma_{12} = \sigma_{21} = 2\left[\overline{\psi}_1 + \overline{\psi}^*_{4f}\kappa_f + \overline{\psi}^*_{4s}(1-2\kappa_s)\right]\gamma + \frac{1}{2}\overline{\psi}_{8fs} \quad (26)$$

Note that although the applied active stress is dispersed along the fiber direction, there are no components of the active stress in the two other orthogonal directions ($\mathbf{s}_0$ and $\mathbf{n}_0$). The Cauchy stress σ_{11} is shown in Figure 4(b) as a function of the amount of shear γ for values κ_f between 1/8 and 1/3 (isotropy). As can clearly be seen from the plots, an increased fiber dispersion decreases the Cauchy stress σ_{11}. In this example, the active stress is zero in the reference configuration and increases with the increase of shear. Also here, a comparison is shown with FE results (the circles in Figure 4(b)) where $\kappa_f = 1/8$.

3.3. Influence of myocyte dispersion on the mechanical tissue response

The influence of the myocyte dispersion on the mechanical tissue response is shown in a purely numerical example by using the same unit myocardium tissue cube (with 10 mm size) as in the previous examples. The cube is discretized by 10 × 10 × 10 FEs with fixed displacement boundary conditions in all DOF on the faces of the cube at $X_2 = 0$ and $X_2 = 10$ mm.

The dispersion parameter κ_s was set to zero. Four different values for κ_f are used (0, 0.1, 0.2, 0.3) while keeping κ_s constant. The cube is activated by a potential of $V_m = +30$ mV, and the corresponding first principal stress σ_I is shown in Figure 5. As can be seen in the figure, an increase in the κ_f-value toward isotropy lowers the value of σ_I and also decreases the contraction in the fiber direction. This is because of the increased dispersion of the fiber direction, which leads to an increase in active stress components along the X_2-direction and X_3-direction and because of the incompressibility of the material, which reduces the influence of the active stress in the fiber direction in that particular example. Thus, this example illustrates the influence dispersion has on the active stress tensor σ_a and the resulting contraction in the material.

3.4. Passive inflation of a ventricular section

A left ventricular slice model is generated by approximating the cross section of the LV by a cylinder, as illustrated in Figure 6(a). Two models, say *A* and *B*, of the same geometry but with different fiber and sheet arrangements are created. In model *A*, the average fiber angle α varies from +60° to −60° and the average sheet angle β varies from +85° to −85° transmurally from the epicardium to the endocardium, where the fiber and sheet angles α and β are defined in Figure 6(b). In Model *B*, the fiber and sheet angles are assumed to be zero. The slice geometry is meshed with 400 hexahedral FEs, which are fixed against translation in the ξ_2-direction at the cut surfaces and in the ξ_3-direction at the epicardial border to hinder rigid body movements. No electrical stimulus was applied, that is, the tissue remained electrically quiescent, and thus no active stresses were generated. Instead, the slice is passively inflated by applying a pressure load of 100 mmHg to the endocardial surface in 200 incremental load steps of equal size. The influence of the dispersion parameters κ_f and κ_s on the distribution of the first principal stress σ_I is investigated by either using the dispersion parameters for healthy and diseased tissues, as provided in Figure 2, or by using the dispersion parameters $\kappa_f = 0.2$ (strongly dispersed) and $\kappa_s = 0$ (perfect alignment), and vice versa.

In Figure 7, the resulting first principal Cauchy stress σ_I at the applied pressure load of 100 mmHg is shown for different dispersion parameters. Figure 7(a) shows the stress distribution by using the dispersion parameters for a healthy myocardium resulting in a band of higher stresses in the middle region of the myocardium. This band is noticeably reduced by using

Europe PMC Funders Author Manuscripts

the dispersion parameters for the fibers related to a diseased myocardium, as shown in Figure 7(b). Instead, stresses are more spread out radially, and at the endocardial border, stresses are higher relative to the setup of Figure 7(a). This suggests that the fiber dispersion alone induces a radial stress gradient where the highest stresses arise at the inner wall, as commonly seen in, for example, pressurized thickwalled isotropic tubes. This is exactly the case when using aligned sheets and a pronounced fiber dispersion, as can be seen in Figure 7(c). In the opposite case, that is, with fiber alignment and a pronounced sheet dispersion, there is an increased stress gradient visible in the middle region of the myocardium, as seen in Figure 7(d).

For the sake of comparison, for model B, the first principal Cauchy stress σ_I at 100 mmHg was computed, and the related results are shown in the Figure 7(e,f) for two sets of dispersion parameters. For the case of a higher dispersion parameter κ_f (relates to a diseased myocardium), the first principal Cauchy stress is slightly higher at the endocardial border. This effect is not so pronounced when comparing Figure 7(a) with (b). It is also clear that the symmetric fiber and sheet angles, used in model A, contribute to the increased mid-myocardial stresses.

3.5. Left ventricle model indicating the influence of fiber and sheet dispersions upon contraction

To study the influence of fiber and sheet dispersions upon contraction over a cardiac cycle, an ellipsoidal model of the LV was constructed; the dimensions correlate with a rabbit LV [35]. The coordinates of the LV are described in prolate spheroidal coordinates with the axes ξ_1, ξ_2, and ξ_3, pointing in the radial, longitudinal, and circumferential directions, respectively. The coordinate system is illustrated in Figure 6(a). The arrangements of the fibers and the sheets correspond to model A, as described in Section 3.4. Pressure boundary conditions, as imposed by the ventricular deformation and the response of the vascular system, are applied on the endocardial surface. The pressure p in the cavity is governed as follows:

1. Non-physiological initial phase with linear pressure increases starting from $p = 0$ to the end diastolic pressure (EDP) ($p = 20$ mmHg).
2. Isochoric LV compression phase, p increases from EDP up to 95 mmHg.
3. Ejection phase where the PV relationship is governed by a Windkessel model, that is,

$$C\frac{\mathrm{d}p}{\mathrm{d}t} + \frac{p}{R} = -\frac{\mathrm{d}V}{\mathrm{d}t} \quad (27)$$

   until reversed blood flow.
4. Isochoric LV relaxation phase, p drops down to 12.5 mmHg.
5. Filling phase with linear pressure increases to EDP.

In steps (2) and (4), the pressure p is computed using the iterative relation $p_{n+1} = p_n + (V_{n+1} - V_n)/C_p$ to keep the cavitary volume V of the LV constant, where C_p serves as a penalty parameter [36]. In step (3), where a two-element Windkessel model is used, the parameters C and R relate to the arterial compliance and the resistance, respectively. The values for C and R are chosen to generate PV loops that match with experimental data of rabbits [37]. Parameters required for calculating the pressure are the following: $C = 0.2$ ml mmHg^{-1}, $R = 700$ mmHg ms ml^{-1}, and $C_p = -900$ ml mmHg^{-1}. The parameters used to describe both active and passive mechanical behaviors of the model are summarized in Table I, except for κ_f and κ_s which correspond to the dispersion parameters given in Figure 2. The mechanical

boundary conditions for the LV are described in Table II. The mesh consists of 5310 hexahedral (mixed) FEs used to solve the mechanics and of 1,201,507 linear hybrid FEs to solve the electrics [38]. The model by Mahajan *et al.* [39] is employed to describe cellular dynamics, where the system of ODEs is solved using the Rush–Larsen algorithm [40] with several optimizations [41]. The model was initialized by pacing a single cell at a pacing cycle length of 350 ms until a stable limit cycle was observed.

The state vector η at the end of this pre-pacing procedure was used to populate the LV model with an initial state vector η_0. Transmembrane current injection applied to the endocardial surface at $t = 0$ ms initiated the propagation of the action potentials at the endocardium to approximate a predominantly transmural activation sequence, as induced by activation via the Purkinje system. In this approximation, the whole endocardium was activated synchronously, electrical activation delays within the endocardium remained unaccounted for. We simulated 350 ms of activity to cover one depolarization and repolarization cycle over the entire LV. The spread of the electrical activation and repolarization is modeled using Equation (19).

By using the dispersion parameters that relate to the healthy and the diseased tissue, as seen in Figure 2, the resulting deformations are quite different. This is illustrated at both the end diastolic volume and the end systolic volume, as shown in the Figure 8(a,b), respectively. Thereby, the distribution of the magnitude of the difference $|\mathbf{u}_H - \mathbf{u}_D|$ between the displacements is shown (H stands for healthy tissue and = diseased). The resulting PV loops obtained from the simulations for different sets of dispersion parameters are shown in Figure 8(c); also, the case for no dispersion is illustrated ($\kappa_f = \kappa_s = 0$). Although only a minor shift in the PV loops between the cases with no dispersions and with fiber and sheet dispersions for a healthy myocardium was observed, a remarkably different behavior is obtained with a fiber dispersion κ_f relating to a diseased myocardium; thereby, the end diastolic and systolic volumes are much larger.

4. DISCUSSION

There are several reports in the literature, which provide evidence for the presence of dispersion in the fiber and sheet orientations in myocardial tissues. Under healthy conditions, dispersion is rather mild, but under certain pathologies such as HCM [13, 42, 43], dispersion can be quite pronounced. In the vast majority of modeling studies, however, dispersion and its influence upon the mechanical response of the myocardium has been largely ignored. In this study, a mechanical model of myocardial tissue has been proposed, which explicitly accounts for the dispersion of fibers and sheets. By changing two scalar (dispersion) parameters, introduced as κ_f and κ_s, the dispersion along the fiber and the sheet direction can be steered independently, thus allowing mechanistic investigations of pathological changes. The independence of the fiber and sheet directions is a reasonable approximation, despite the microstructural interaction. An approach that couples the fiber and sheet orientations is feasible; however, specific data are missing. The dispersion parameters κ_f, κ_s determine the blend between the isotropy (characterized by the invariant I_1) and the transverse isotropy (characterized by the invariants I_{4f}, I_{4s}). Thus, together, they give a dispersed orthotropic structure response where an increased dispersion leads to a more isotropic active and passive mechanical response.

The analytical and numerical examples investigated in this study suggest that dispersion may be an important factor in cardiac electromechanics. The increase in the dispersion along the fiber direction showed the most striking effect. This is illustrated in, for example, Figure 5 where the increase in the dispersion reduces contraction and the first principal stress. The enforced incompressibility condition is responsible for this reduced contraction, as can be

seen from the analytical expressions (20)–(22) and (24)–(26). From a physiological point of view, there is also an interpretation. As the dispersion increases, the orientation of myocytes, which are responsible for active contraction, becomes more evenly distributed. When dispersion is large enough, there is no preferred myocyte orientation anymore. This would entail an isotropic contraction, which is, however, impossible without altering the volume. Moreover, besides distributing the direction of active contraction, fiber dispersion also has a major impact on the passive myocardial response. This is illustrated in Figure 7(a)–(c) where the fiber dispersion is increased in a ventricular slice model. During passive inflation of the slice, the first principal stress changes from being elevated in a mid-myocardial band for low fiber dispersion to being elevated at the endocardial border for high fiber dispersion. This shift is similar to what is commonly seen when inflating a thick-walled tube.

Although the effects of dispersion in the fiber direction on the mechanical myocardial response is more striking, numerical results indicate that increases in the sheet dispersion lead to significant alterations in the model behavior as well. The overall material response changes gradually from orthotropic toward transversely isotropic where the sheet response becomes indistinguishable from the sheet-normal response. This can be seen either in the analytical part of the first example discussed in Section 3.1, see equations (21) and (22), where $\kappa_s = 1/3$ gives identical expressions for the Cauchy stresses σ_{22} and σ_{33}, or, alternatively, from Figure 3(c) where the behavior is identical along the sheet and sheet-normal directions. The difference in the passive stress response between a (nearly) transversely isotropic and an orthotropic material can be appreciated by comparing Figure 7(d) with Figure 7(a), where the stress in the middle region of the myocardium is even more elevated for the (nearly) transversely isotropic material. This large difference in the stress response also highlights the importance of the orthotropic structure as a factor that has to be considered when simulating ventricular electromechanical problems. Residual stresses, however, has not been included in the simulation, why the particular stress distribution, as shown in Figure 7, should not be considered as the true stress in a ventricle. It merely shows how the fiber and sheet dispersions affect the stress distribution.

Section 3.5 illustrates the numerical results for an electromechanically coupled model of the LV from a rabbit for a healthy and a pathological myocardium. Although the effects of using fiber and sheet dispersion parameters for the healthy myocardium were fairly minor, the use of fiber dispersions relating to a pathological myocardium had a rather big effect. As can be seen by comparing the PV loops in Figure 8(c), a significant shift of the entire PV loop toward larger end diastolic and end systolic LV cavity volumes occurred. Although the PV loops show that there is a difference in volume of the ventricular lumen, Figure 8(a,b) also illustrate that the remaining ventricular wall undergoes different patterns of deformation when using different dispersion parameters.

In summary, our modeling results identified the fiber and sheet dispersions as important determinants for the electromechanics of the myocardium. Distributed fiber and sheet orientations should be considered for more reliable predictions of, for example, stress, deformation, and volume change, in particular when compared with experimental data obtained from a pathological myocardium.

Limitations of the study

Because of the lack of structural data of pathological myocardium, it is difficult to find suitable comparisons on which we may validate our approach. Therefore, we have focused on the description of the dispersion model and have attempted to show the related mechanisms. Once adequate structural data exist, future work is needed to validate and modify the model if necessary.

Europe PMC Funders Author Manuscripts

The fit of the histogram data to the PDF assumes a bell-shaped data distribution. This may not be suitable in pathological cases with increased fiber dispersion. As shown in Figure 2(b), which displays the fiber dispersion of an HCM-diseased tissue, there may exist two predominant myocyte orientations in the region of interest. It is certainly possible to retrieve individual dispersion parameters; however, the increased dispersion obtained from the HCM sample was only seen within small focal islands throughout the myocardial wall [7, 8]. To appropriately account for the bimodal distribution of orientations, higher spatial resolutions would be required than those commonly used within FE studies, including this study. Because the spatial extent of a single FE in the models used exceeds the size of a focal island in which increased dispersion can be found, we opted to only use one average direction that corresponds to a fit of the bell-shaped function over both predominant orientations.

In the LV model discussed in Section 3.5, the dispersion parameters corresponding to the tissue diseased by HCM were used throughout the entire LV wall. This is not a realistic assumption as the dispersion in the smaller focal islands seems only to be present at approximately 25% of the overall LV volume [7, 8]. Available data show sheet and fiber dispersions averaged over all islands found in a given ventricle, but no data on the spatial distribution and morphology of such islands are available. Therefore, simulation results show an overly diseased case that can be considered as a limiting case for the dispersion effects. However, the focus of this study is mainly on the description of the modeling procedure and the potential effects of fiber dispersion and not on the development of a model that strives for a perfect pathophysiological match for an HCM-diseased LV. In future higher resolution FE-modeling studies, dispersion parameters may easily be set to vary from FE to element; however, by considering the paucity of available data on the spatial dispersion variation, such a detailed investigation would appear to be premature. Experimental studies that characterize spatial and morphological aspects of the dispersion over the entire myocardium in health and disease are, therefore, of utmost need to provide a more solid basis for a more detailed study aiming to provide more specific predictions.

Because of the limited experimental data available, we were not able to use data from one species only. For example, it was necessary to retrieve the dispersion data from a rat myocardium [7, 16], whereas passive material parameters were retrieved from a porcine myocardium [44]. However, this limitation does not affect the qualitative conclusions drawn from using the proposed dispersed formulation for myocardium.

Furthermore, in the LV model, the parameters κ_f and κ_s affected only the mechanical response of the LV but not the electrical activation sequence because dispersion remained unaccounted for in the mono-domain equation. That is, the orthotropy in the propagation of the action potential in the LV model was governed by the mean orientation of the fibers and the sheets. A consideration of the dispersion in the electrical model would also reduce the orthotropy. However, the chosen activation sequence, which approximates a normal beat where the entire endocardium is activated almost simultaneously, leads to a strongly transmural activation where effects of electrical orthotropy are strongly attenuated. Under such conditions, the consequence of electrical dispersion is minor and can be neglected, particularly when considering the rather large uncertainty in the experimental reports on conductivity values, which vary up to 300% [45].

Acknowledgments

The authors wish to thank Professor Ray W. Ogden from the University of Glasgow for the productive discussions. This project was partly supported by the SFB Research Center ‘Mathematical Optimization and Applications in Biomedical Sciences’, project F3210-N18 granted by the Austrian Science Fund. This support is gratefully acknowledged.

APPENDIX A: ELASTICITY TENSORS FOR THE ACTIVE STRESS

Using the definition $\mathbf{M}_0 := \mathbf{f}_0 \otimes \mathbf{f}_0$ and the abbreviation (15), (14) may be written as

$$\mathbf{S}_{\mathrm{a}} = S_{\mathrm{a}} \left(\frac{\kappa_{\mathrm{f}}}{1-2\kappa_{\mathrm{f}}} \mathbf{C}^{-1} + \frac{1-3\kappa_{\mathrm{f}}}{1-2\kappa_{\mathrm{f}}} I_{4\mathrm{f}}^{-1} \mathbf{M}_0 \right) \quad (28)$$

The Lagrangian elasticity tensor is given by $\mathbb{C}_a = 2\partial \mathbf{S}_{\mathrm{a}} / \partial \mathbf{C}$ which leads to

$$\mathbb{C}_{\mathrm{a}} = 2 \frac{S_{\mathrm{a}}}{1-2\kappa_{\mathrm{f}}} \left[\kappa_{\mathrm{f}} \frac{\partial \mathbf{C}^{-1}}{\partial \mathbf{C}} + (1-3\kappa_{\mathrm{f}}) \frac{\partial I_{4\mathrm{f}}^{-1} \mathbf{M}_0}{\partial \mathbf{C}} \right] \quad (29)$$

Using the derivative $\partial \left(I_{4\mathrm{f}}^{-1} \mathbf{M}_0 \right) / \partial \mathbf{C} = -I_{4\mathrm{f}}^{-2} \mathbf{M}_0 \otimes \mathbf{M}_0$ (29) can be written as

$$\mathbb{C}_{\mathrm{a}} = 2 \frac{S_{\mathrm{a}}}{1-2\kappa_{\mathrm{f}}} \left[\kappa_{\mathrm{f}} \frac{\partial \mathbf{C}^{-1}}{\partial \mathbf{C}} - (1-3\kappa_{\mathrm{f}}) I_{4\mathrm{f}}^{-2} \mathbf{M}_0 \otimes \mathbf{M}_0 \right] \quad (30)$$

and by using the push-forward operation of $\mathbb{C}_{\mathrm{a}}$ according to $[\mathbb{C}_{\mathrm{a}}]_{abcd} = J^{-1} F_{aA} F_{bB} F_{cC} F_{dD} [\mathbb{C}_{\mathrm{a}}]_{ABCD}$, this leads to the Eulerian elasticity tensor

$$\mathbb{C}_{\mathrm{a}} = -2 \frac{S_{\mathrm{a}}}{J(1-2\kappa_{\mathrm{f}})} \left[\kappa_{\mathrm{f}} \mathbb{I} + (1-3\kappa_{\mathrm{f}}) \widehat{\mathbf{M}} \otimes \widehat{\mathbf{M}} \right. \quad (31)$$

where the fourth-order identity tensor $\mathbb{I}$ defined in index notation as $[\mathbb{I}]_{abcd} = (\delta_{ac}\delta_{bd} + \delta_{ad}\delta_{cd})/2$, is introduced from the push-forward relation $F_{aA} F_{bB} F_{cC} F_{dD} \left[\partial \left(\mathbf{C}^{-1} \right) / \partial \mathbf{C} \right]_{ABCD} = -[\mathbb{I}]_{abcd}$ and the definition $\widehat{\mathbf{M}} := \mathbf{F} \mathbf{I}_{4\mathrm{f}}^{-1} \mathbf{M}_0 \mathbf{F}^{\mathbf{T}} = \hat{\mathbf{f}} \otimes \hat{\mathbf{f}}$ has been used.

REFERENCES

1. Streeter DD Jr. Spotnitz HM, Patel DP, Ross J Jr. Sonnenblick EH. Fibre orientation in the canine left ventricle during diastole and systole. Circulation Research. 1969; 24:339–347. [PubMed: 5766515]
2. Usyk TP, Mazhari R, McCulloch AD. Effect of laminar orthotropic myofiber architecture on regional stress and strain in the canine left ventricle. Journal of Elasticity. 2000; 61:143–164.
3. Rohmer D, Sitek A, Gullberg GT. Reconstruction and visualization of fiber and laminar structure in the normal human heart from ex vivo diffusion tensor magnetic resonance imaging (DTMRI) data. Investigative Radiology. 2007; 42:777–789. [PubMed: 18030201]
4. LeGrice IJ, Smaill BH, Chai LZ, Edgar SG, Gavin JB, Hunter PJ. Laminar structure of the heart: ventricular myocyte arrangement and connective tissue architecture in the dog. The American Journal of Physiology. 1995; 269:H571–H582. [PubMed: 7653621]
5. Young AA, Legrice IJ, Young MA, Smaill BH. Extended confocal microscopy of myocardial laminae and collagen network. Journal of Microscopy. 1998; 192:139–150. [PubMed: 9853371]
6. Sands GB, Gerneke DA, Hooks DA, Green CR, Smaill BH, LeGrice IJ. Automated imaging of extended tissue volumes using confocal microscopy. Microscopy Research and Technique. 2005; 67:227–239. [PubMed: 16170824]
7. Karlon WJ, Covell JW, McCulloch AD, Hunter JJ, Omens JH. Automated measurement of myofiber disarray in transgenic mice with ventricular expression of ras. Anatomical Record. 1998; 252:612–625. [PubMed: 9845212]

8. Karlon WJ, McCulloch AD, Covell JW, Hunter JJ, Omens JH. Regional dysfunction correlates with myofiber disarray in transgenic mice with ventricular expression of ras. American Journal of Physiology: Heart and Circulatory Physiology. 2000; 278:H898–906. [PubMed: 10710359]
9. Usyk TP, Omens JH, McCulloch AD. Regional septal dysfunction in a three-dimensional computational model of focal myofiber disarray. American Journal of Physiology: Heart and Circulatory Physiology. 2001; 281:H506–H514. [PubMed: 11454551]
10. Whittaker P, Boughner DR, Kloner RA. Analysis of healing after myocardial infarction using polarized light microscopy. American Journal of Pathology. 1989; 134:879–893. [PubMed: 2705508]
11. Zimmerman SD, Karlon WJ, Holmes JW, Omens JH, Covell JW. Structural and mechanical factors influencing infarct scar collagen organization. American Journal of Physiology: Heart and Circulatory Physiology. 2000; 278:H194–H200. [PubMed: 10644599]
12. Strijkers GJ, Bouts A, Blankesteijn WM, Peeters THJM, Vilanova A, van Prooijen MC, Sanders HMHF, Heijman E, Nicolay K. Diffusion tensor imaging of left ventricular remodeling in response to myocardial infarction in the mouse. NMR in Biomedicine. 2009; 22:182–190. [PubMed: 18780284]
13. Tseng WYI, Dou J, Reese TG, Wedeen VJ. Imaging myocardial fiber disarray and intramural strain hypokinesis in hypertrophic cardiomyopathy with MRI. Journal of Magnetic Resonance Imaging. 2006; 23:1–8. [PubMed: 16331592]
14. Coppola BA, Omens JH. Role of tissue structure on ventricular wall mechanics. Molecular and cellular biomechanics. 2008; 5:183–196. [PubMed: 18751527]
15. Hooks DA, Trew ML, Caldwell BJ, Sands GB, LeGrice IJ, Smaill BH. Laminar arrangement of ventricular myocytes influences electrical behavior of the heart. Circulation Research. 2007; 101:e103–e112. [PubMed: 17947797]
16. Covell JW. Tissue structure and ventricular wall mechanics. Circulation. 2008; 118:699–701. [PubMed: 18695201]
17. Sands GB, Smaill BH, LeGrice IJ. Virtual sectioning of cardiac tissue relative to fiber orientation. Conf Proc IEEE Eng Med Biol Soc. 2008:226–229. [PubMed: 19162634]
18. Holzapfel GA, Ogden RW. Constitutive modelling of passive myocardium: a structurally based framework for material characterization. Philos Trans A Math Phys Eng Sci. 2009; 367:3445–3475. [PubMed: 19657007]
19. Gasser TC, Ogden RW, Holzapfel GA. Hyperelastic modelling of arterial layers with distributed collagen fibre orientations. J R Soc Interface. 2006; 3:15–35. [PubMed: 16849214]
20. Ambrosi D, Pezzuto S. Active stress vs. active strain in mechanobiology: constitutive issues. Journal of Elasticity. 2012; 107:199–212.
21. Niederer SA, Smith NP. An improved numerical method for strong coupling of excitation and contraction models in the heart. Progress in Biophysics and Molecular Biology. 2008; 96:90–111. [PubMed: 17881038]
22. Holzapfel GA, Ogden RW. Constitutive modelling of arteries. Proceedings of the Royal Society A. 2010; 466:1551–1597.
23. Holzapfel, GA. Nonlinear Solid Mechanics. A Continuum Approach for Engineering. John Wiley & Sons; Chichester: 2000.
24. Pierce DM, Trobin W, Raya JG, Trattnig S, Bischof H, Glaser C, Holzapfel GA. DT-MRI based computation of collagen fiber deformation in human articular cartilage: a feasibility study. Annals of Biomedical Engineering. 2010; 38:2447–2463. [PubMed: 20225124]
25. Nash MP, Panfilov AV. Electromechanical model of excitable tissue to study reentrant cardiac arrhythmias. Progress in Biophysics and Molecular Biology. 2004; 85:501–522. [PubMed: 15142759]
26. Göktepe S, Kuhl E. Electromechanics of the heart: a unified approach to the strongly coupled excitation-contraction problem. Computational Mechanics. 2010; 45:227–243.
27. FEAP-A Finite Element Analysis Program, Version 8.2 User Manual. University of California at Berkeley; Berkeley, California: 2008.

28. Colli Franzone P, Pavarino LF, Taccardi B. Simulating patterns of excitation, repolarization and action potential duration with cardiac bidomain and monodomain models. Mathematical Biosciences. 2005; 197:35–66. [PubMed: 16009380]
29. Nielsen BF, Ruud TS, Lines GT, Tveito A. Optimal monodomain approximations of the bidomain equations. Applied Mathematics and Computation. 2007; 184:276–290.
30. Prassl AJ, Kickinger F, Ahammer H, Grau V, Schneider JE, Hofer E, Vigmond EJ, Trayanova NA, Plank G. Automatically generated, anatomically accurate meshes for cardiac electrophysiology problems. IEEE Transactions on Bio-medical Engineering. 2009; 56:1318–1330. [PubMed: 19203877]
31. Karypis, G.; Schloegel, K.; Kumar, V. ParMETIS: Parallel Graph Partitioning and Sparse Matrix Ordering Library. University of Minnesota; Minneapolis, MN: 2003. Version 3.1Available from: http://glaros.dtc.umn.edu/gkhome/metis/parmetis/overview [Accessed on 25 June 2013]
32. Balay, S.; Brown, J.; Buschelman, K.; Eijkhout, V.; Gropp, WD.; Kaushik, D.; Knepley, MG.; Curfman McInnes, L.; Smith, BF.; Zhang, H. Technical Report. Argonne National Laboratory; 2010. PETSc users manual.
33. Vigmond EJ, Hughes M, Plank G, Leon LJ. Computational tools for modeling electrical activity in cardiac tissue. Journal of Electrocardiology. 2003; 36(Suppl):69–74. [PubMed: 14716595]
34. Vigmond EJ, Weber dos Santos R, Prassl AJ, Deo M, Plank G. Solvers for the cardiac bidomain equations. Progress in Biophysics and Molecular Biology. 2008; 96:3–18. [PubMed: 17900668]
35. Vetter FJ, McCulloch AD. Three-dimensional analysis of regional cardiac function: a model of the rabbit ventricular anatomy. Progress in Biophysics and Molecular Biology. 1998; 69:157–183. [PubMed: 9785937]
36. Usyk TP, LeGrice IJ, McCulloch AD. Computational model of three-dimensional cardiac electromechanics. Computing and Visualization in Science. 2002; 4:249–257.
37. Royse CF, Royse AG. The myocardial and vascular effects of bupivacaine, levobupivacaine, and ropivacaine using pressure volume loops. Anesthesia and Analgesia. 2005; 101:679–687. [PubMed: 16115975]
38. Rocha BM, Kickinger F, Prassl AJ, Haase G, Vigmond EJ, Weber dos Santos R, Plank SZG. A macro finite-element formulation for cardiac electrophysiology simulations using hybrid unstructured grids. IEEE Transactions on Bio-medical Engineering. 2011; 58:1055–1065. [PubMed: 20699206]
39. Mahajan A, Shiferaw Y, Sato D, Baher A, Olcese R, Xie LH, Yang MJ, Chen PS, Restrepo JG, Karma A, Garfinkel A, Qu Z, Weiss JN. A rabbit ventricular action potential model replicating cardiac dynamics at rapid heart rates. Biophysical Journal. 2008; 94:392–410. [PubMed: 18160660]
40. Rush S, Larsen H. A practical algorithm for solving dynamic membrane equations. IEEE Transactions on Bio-medical Engineering. 1978; 25:389–392. [PubMed: 689699]
41. Plank G, Zhou L, Greenstein JL, Cortassa S, Winslow RL, O'Rourke B, Trayanova NA. From mitochondrial ion channels to arrhythmias in the heart: computational techniques to bridge the spatio-temporal scales. Philos Trans A Math Phys Eng Sci. 2008; 366:3381–3409. [PubMed: 18603526]
42. Dong SJ, MacGregor JH, Crawley AP, McVeigh E, Belenkie I, Smith ER, Tyberg JV, Beyar R. Left ventricular wall thickness and regional systolic function in patients with hypertrophic cardiomyopathy. A three-dimensional tagged magnetic resonance imaging study. Circulation. 1994; 90:1200–1209. [PubMed: 8087929]
43. Carasso S, Yang H, Woo A, Vannan MA, Jamorski M, Wigle ED, Rakowski H. Systolic myocardial mechanics in hypertrophic cardiomyopathy: novel concepts and implications for clinical status. Journal of the American Society of Echocardiography. 2008; 21:675–683. [PubMed: 18187306]
44. Dokos S, Smaill BH, Young AA, LeGrice IJ. Shear properties of passive ventricular myocardium. American Journal of Physiology. 2002; 283:H2650–H2659. [PubMed: 12427603]
45. Roth BJ. Electrical conductivity values used with the bidomain model of cardiac tissue. IEEE Transactions on Bio-medical Engineering. 1997; 44:326–328. [PubMed: 9125816]

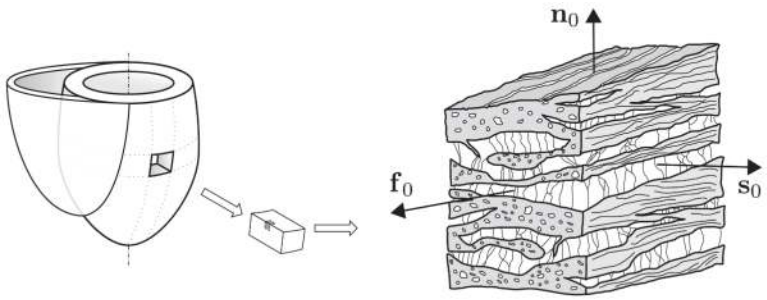

Figure 1.
Schematic representation of the structure of the myocardium showing the fiber-reinforced laminar composite that comprises the averaged fiber, sheet, and sheet-normal directions in a continuum model, characterized by $\mathbf{f}_0$, $\mathbf{s}_0$, and $\mathbf{n}_0$, respectively.

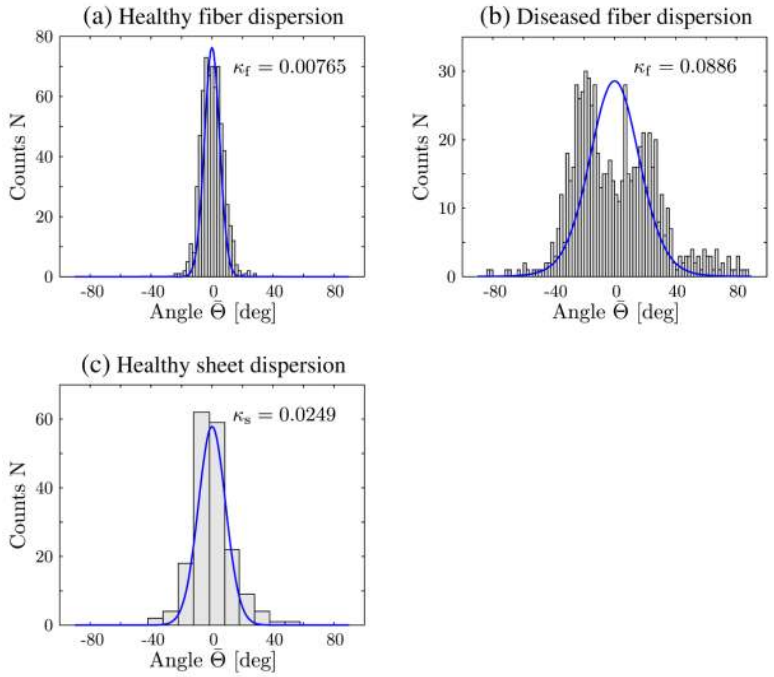

Figure 2.
Fit of histogram data for fiber and sheet dispersions adapted from [7, 16], (a) fiber dispersion in a healthy tissue ($\kappa_f = 0.00765$); (b) fiber dispersion in a diseased tissue ($\kappa_f = 0.0886$); and (c) sheet dispersion in a healthy tissue ($\kappa_s = 0.0249$).

Europe PMC Funders Author Manuscripts

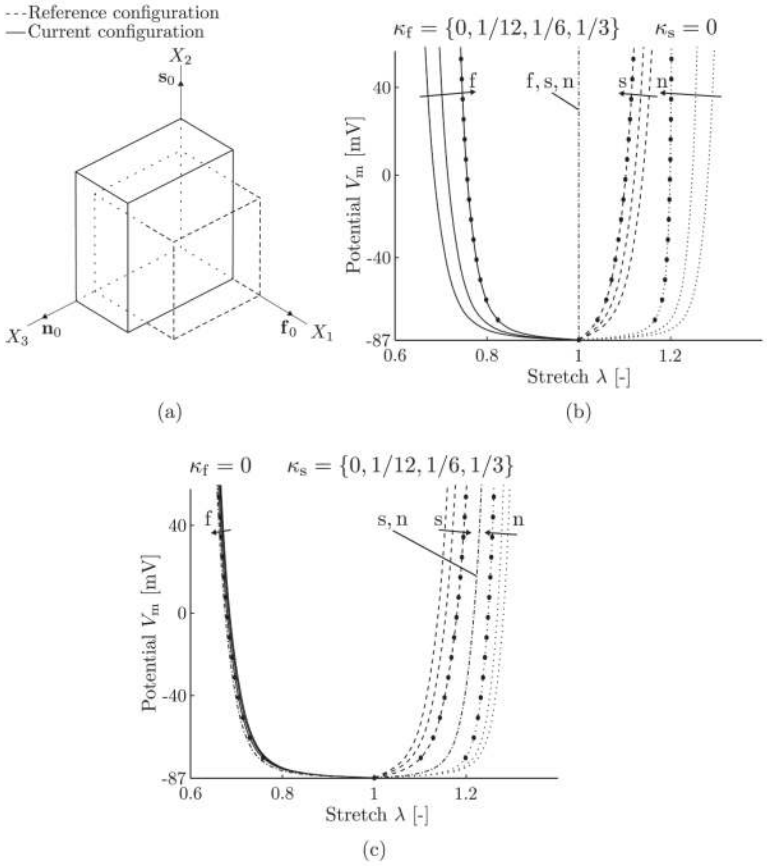

Figure 3.

(a) Deformation of a unit cube when activated in the fiber direction; analytical results along the fiber, sheet, and sheet-normal directions using different values for the distribution parameters κ_f in (b) and κ_s in (c). The fiber, sheet, and sheet-normal responses are shown by solid, dashed, and dotted curves, respectively, and the circles show the finite element results for comparison reasons using either $\kappa_f = 1/6$, see (b), or $\kappa_s = 1/6$, see (c). Using the limiting case $\kappa_f = 1/3$ or $\kappa_s = 1/3$, the dash-dotted curves show the stretch responses for all three f, s, and n-directions, see (b), and for the s and n-directions, see (c).

Europe PMC Funders Author Manuscripts

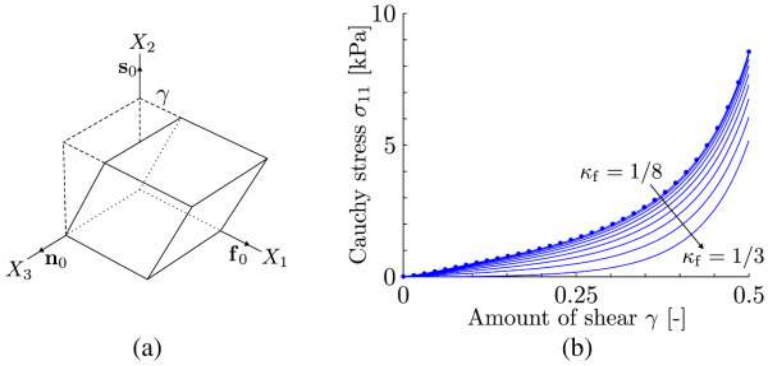

Figure 4.

(a) Simple shear deformation of a unit cube with the deformation gradient $\mathbf{F} = \mathbf{I} + \gamma \mathbf{f}_0 \otimes \mathbf{s}_0$; (b) Cauchy stress σ_{11} versus the amount of shear γ for values κ_f between 1/8 and 1/3. The show FE results for comparison reasons using $\kappa_f = 1/8$.

Europe PMC Funders Author Manuscripts

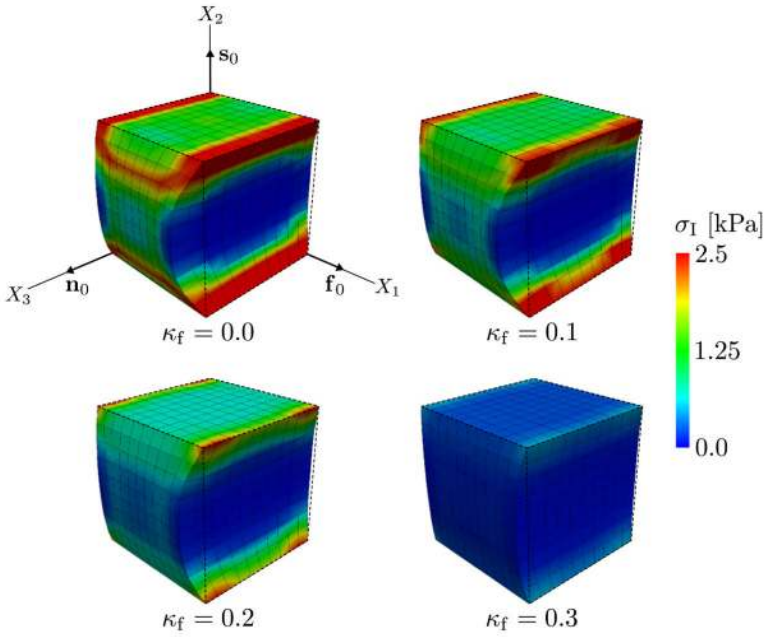

Figure 5.
Cube of myocardial tissue subjected to an active stress corresponding to a potential of +30 mV with the dispersion parameters $\kappa_f = \{0, 0.1, 0.2, 0.3\}$ and $\kappa_s = 0$. The images illustrate the corresponding first principal stress σ_I.

Europe PMC Funders Author Manuscripts

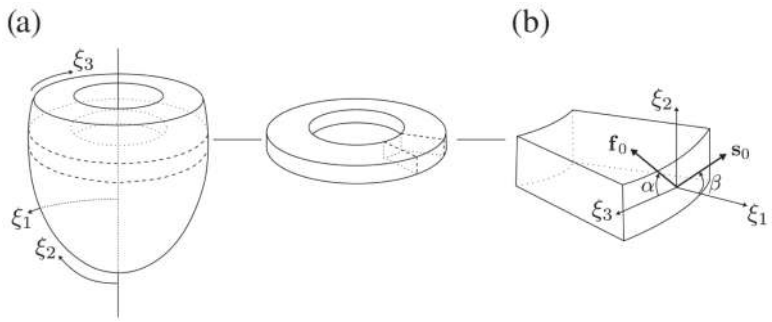

Figure 6.
(a) Coordinate system of the left ventricle model and a section of the left ventricle; (b) average fiber orientation defined by the angle α in the (ξ_2, ξ_3)-plane, and average sheet orientation defined by the angle β in the (ξ_1, ξ_2)-plane. The arrows point in the positive directions of the angles.

Europe PMC Funders Author Manuscripts

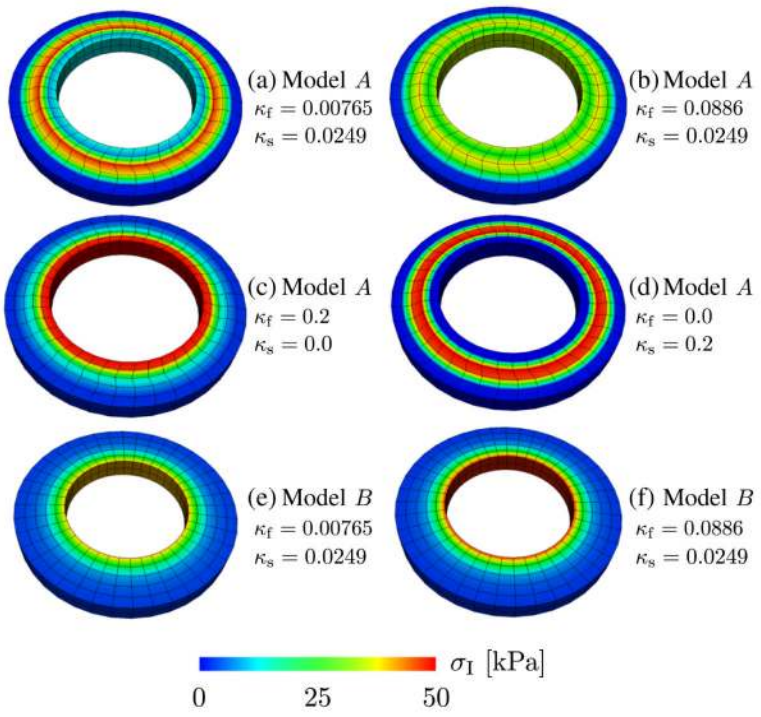

Figure 7.
Distribution of the first principal stress σ_I at applied pressure load of 100 mmHg in a section of a ventricular model. Models A and B pertain to different fiber and sheet-orientations; Model A: $-60° \leq \alpha \leq +60°$ and $-85° \leq \beta \leq +85°$; Model B: $\alpha = \beta = 0$ (α and β denote fiber and sheet angles, respectively, as defined in Figure 6(b)). For some dispersion parameters, see Figure 2.

Europe PMC Funders Author Manuscripts

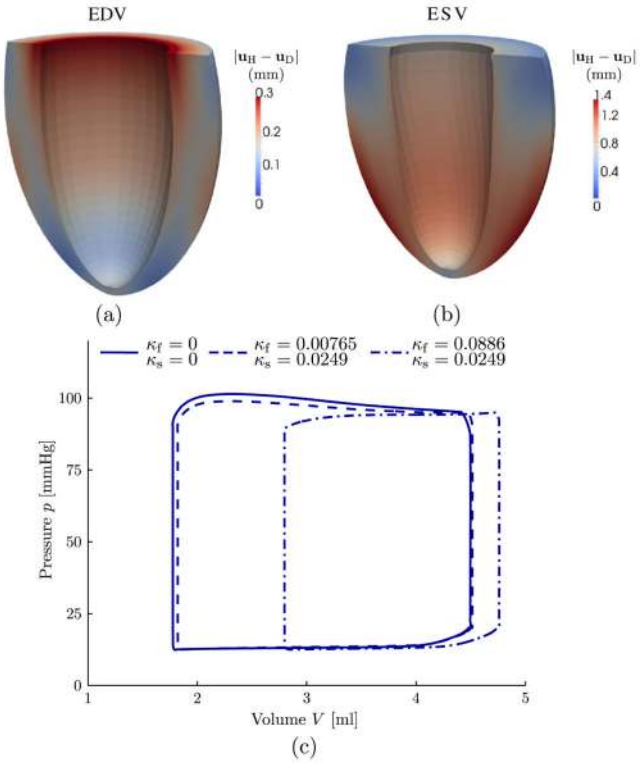

Figure 8.
Magnitude of the difference $|\mathbf{u}_H - \mathbf{u}_D|$ between the displacements (H stands for healthy tissue and D for diseased) for (a) the end diastolic volume (EDV) and (b) the end systolic volume (ESV). (c) Pressure–volume loops for different sets of dispersion parameters κ_f and κ_s.

Europe PMC Funders Author Manuscripts

Table I

Material parameters used for both analytical and numerical calculations, except for the dispersion values of κ_f and κ_s, which are provided in the respective section. The material parameters for the passive tissue behavior are taken from [18], whereas the parameters for the active stress are taken from [25].

Passive stress		
$\mu_K = 3333$ kPa	$a = 0.333$ kPa	$b = 9.242$ (–)
	$a_f = 18.535$ kPa	$b_f = 15.972$ (–)
	$a_s = 2.564$ kPa	$b_s = 10.446$ (–)
	$a_{fs} = 0.417$ kPa	$b_{fs} = 11.602$ (–)

Active stress		
$\kappa_{S_a} = 0.50$ kPa mV^{-1}	$V_r = -86.796$ mV	$V_s = -80.0$ mV
$\epsilon_0 = 1.0$ ms^{-1}	$\epsilon_\infty = 0.1$ ms^{-1}	$\zeta_r = 0.1$ mV^{-1}

Table II

Mechanical boundary conditions (BCs) for the left ventricle in terms of the prescribed traction **t**, where t_n is a component of **t** normal to the endocardial surface on which the pressure p acts and the displacement **u** with components $u_{\xi 1}$, $u_{\xi 2}$, $u_{\xi 3}$ in the direction of the coordinates given in Figure 6(a).

BCs	Coordinates		Description
$t_n = -p$	$\xi_1 = \xi_{1\,\min}$	For all ξ_2, ξ_3	Endocardial surface
$u_{\xi 2} = 0$	$\xi_2 = \xi_{2\max}$	For all ξ_1, ξ_3	Basal surface
$u_{\xi 3} = 0$	$\xi_1 = \xi_{1\,\max}$ $\xi_2 = \xi_{2\max}$	For all ξ_3	Outer boundary at the base surface